Comparison of ICON-EUV F-Peak Characteristic Parameters with External Data Sources

Gilles Wautelet[1] · Benoît Hubert[1] · Jean-Claude Gérard[1] · Thomas J. Immel[2] · Martin M. Sirk[2] · Eric J. Korpela[2] · Andrew W. Stephan[3] · Stephen B. Mende[2] · Scott L. England[4] · Philip J. Erickson[5]

Abstract

We provide the first comparison of the ICON-EUV O^+ density profile with radio wave datasets coming from GNSS radio-occultation, ionosondes and incoherent scatter radar. The peak density and height deduced from those different observation techniques are compared. It is found that the EUV-deduced peak density is smaller than that from other techniques by 50 to 60%, while the altitude of the peak is retrieved with a slight bias of 10 to 20 km on average. These average values are found to vary between November 2019 and March 2021. Magnetic latitude and local time are not factors significantly influencing this variability. In contrast, the EUV density is closer to that deduced from radio-wave techniques in the mid latitude region, *i.e.* where the ionospheric crests do not play a role. The persistent very low solar activity conditions prevailing during the studied time interval challenge the EUV O^+ density profile retrieval technique. These values are consistent, both in magnitude and direction, with a systematic error on the order of 10% in the data or the forward model, or a combination of both. Ultimately, the EUV instrument on-board ICON provides the only known technique capable of precisely monitoring the ionospheric peak properties at daytime from a single space platform, on a global scale and at high cadence. This feature paves the way to transpose the technology to the study of the ionosphere surrounding other planets.

The Ionospheric Connection Explorer (ICON) Mission: First Results
Edited by David E. Siskind and Ruth S. Lieberman

✉ G. Wautelet
   gilles.wautelet@uliege.be

[1] Laboratory of Planetary and Atmospheric Physics, Liège University, Allée du Six Août, 19C, Liège, Belgium

[2] Space Sciences Laboratory, University of California, Berkeley, CA, USA

[3] U.S. Naval Research Laboratory, Washington D.C., USA

[4] Aerospace & Ocean Engineering, Virginia Tech, Blacksburg, VA, USA

[5] Haystack Observatory, Massachusetts Institute of Technology, Westford, MA, USA

1 Introduction

The electron density in the ionosphere impacts the propagation of the electromagnetic waves crossing this environment. Its important variability in time and space is responsible for large gradients that result in abrupt changes of the refractive index, causing numerous technological issues, e.g. the positioning error using Global Navigation Satellite Systems (GNSS), mainly due to small-scale irregularities in the ionospheric plasma. Such irregularities refract and scatter the GNSS signals, causing the so-called scintillations that make receivers lose lock on the signal or produce incorrect measurements of the signal phase. Ionospheric scintillations span a large range of scale sizes and are more common at low and high geomagnetic latitudes, although they do occur as well at mid-latitudes. In the polar areas, they are caused by electron precipitation due to particle acceleration events ultimately powered by solar activity bursts in the solar wind. At equatorial latitudes, the post-sunset enhancement in electron density is an important physical mechanism providing significant impacts to the energy and momentum budget of the ionosphere. Regular monitoring of electron density profile dynamics therefore provides a key asset for understanding of the physical processes shaping the ionosphere.

On October 11 2019, NASA's ICON satellite was launched into a circular orbit at about 590 km altitude, at 27° inclination. The spacecraft carries four scientific instruments dedicated to the study of the dynamic coupling between the lower atmosphere, the upper atmosphere and the solar environment, including radiation. Among them, two instruments are designed to sense to O^+ density from the bottom of the ionosphere to approximately the spacecraft altitude. First, the Far Ultraviolet Imaging Spectograph (FUV) simultaneously measures the OI–135.6 nm emission of atomic oxygen and the Lyman-Birge-Hopfield (LBH) band of N_2 near 157 nm (Mende et al. 2017). During nighttime, the 135.6 nm channel is used alone to infer the O^+ density profile by observing the radiative recombination of oxygen ions with ambient electrons (Kamalabadi et al. 2018). On the dayside, both the 135.6 nm and LBH emissions are measured and combined to determine O and N_2 altitude profiles and column O/N_2, used to monitor the atmospheric composition changes (Stephan et al. 2018). The comparison of FUV ionospheric peak characteristics with external datasets has been performed by Wautelet et al. (2021) and has inspired the work carried in this present paper, solely based on the second UV instrument, the Extreme Ultra Violet (EUV) spectrograph. EUV records daytime limb altitude profiles of terrestrial emissions in the extreme ultraviolet spectrum from 54 to 88 nm (Sirk et al. 2017), contributing to the ICON mission goal to collect collocated measurements of the upper atmosphere. The OII–61.7 nm and 83.4 nm emissions are used to retrieve daytime O^+ altitude profiles (Stephan et al. 2017). Contrary to FUV, EUV records a single profile of a full spectrum, against two wavelengths for a full imaging capability for FUV. While the common goal of both instruments is the computation of the O^+ density profile, their retrieval method strongly differs as FUV uses a single optically thin emission (the OI–135.6 nm line) while two oxygen emission features are used for EUV, one that is optically thin and one that is not. This adds an additional consideration to the O^+ density profile retrieved from the EUV in that any relative calibration errors between the two colors can create an additional systematic error in the retrieved ionospheric density. Let us also remind that FUV measures the O^+ density during nighttime, while EUV measures it daytime, *i.e.* during conditions where larger O^+ gradients occur, especially around the equatorial anomaly crests.

Simultaneously with the ICON program, the radio-occultation space mission program COSMIC-2 (C2) currently provides several thousands of electron density profiles daily distributed across the globe since October 2019. The six low earth orbiters (LEOs) of the C2

mission record GNSS signals during atmospheric occultations to retrieve ionospheric and neutral atmosphere profiles. Additionally, ground-based ionosondes and incoherent scatter radars (ISRs) perform precise and accurate sets of ionospheric plasma parameters, including the electron density profile, in a local and regional area from facilities distributed over the world. When taken as a whole, such datasets (C2, ionosonde and ISRs) constitute an important database that can be used as comparisons to the ICON-EUV measurements, for the purpose of determination of relative biases in the profiles, and specifically in the F-peak parameters. It is noted here that the requirements for closing the ICON science questions require measurements with precision in N_mF_2 and h_mF_2 for peak density and altitude, respectively, to allow for identification in relative changes in these ionospheric conditions. In contrast, the accuracy of the products that is being assessed in this work will enable enhanced scientific studies beyond the primary goals of the ICON mission. The results of this work will also be vital contributions to the ongoing evaluation of sensor calibration, fundamental cross sections within the modeling and analysis of the emissions, and other potential systematic offsets that may be present in the data and results.

This paper is one of three – in this issue – related to the performance of the ICON EUV. Korpela et al. (in prep.) have provided a review of the performance of the ICON EUV instrument. Stephan et al. (2022) have provided a review of the retrieved Level 2 ionospheric data products and the performance of the retrieval algorithm. This study aims to compare O^+ density profiles obtained by different techniques at the F_2-peak level using its main characteristics N_mF_2 and h_mF_2. The comparison does not focus on the bottomside altitude profile part (lower than the peak) because EUV only observes the atomic ion O^+ while other techniques perform measurements of the electron density (N_e). The latter can strongly differ from the O^+ density in the lower ionosphere due to increasing NO^+ and O_2^+ ion contributions that are not detectable by EUV. After introducing the different measurement techniques used in this work, we compare characteristics of the F_2-peak obtained from EUV and the other data sources. We search for the geographic and temporal conjunctions between EUV and external datasets. While the C2 data set is continuous in time, ionosonde and ISR data are punctual. Indeed, ionosonde data need manual intervention to guarantee their quality, which is very time consuming. Additionally, the ISR of Millstone Hill (MLH), which is the only radar considered in this study, operates in a "campaign" mode, which restricts the size of the EUV-ISR comparison dataset. The found differences and similarities are then discussed, to serve as a basis for future improvements to the accuracy of ionospheric products that will enable future studies beyond the scope that the ICON EUV measurements currently target.

2 Instruments and Methodology

In 2021, a comparison work assessing the performance of the ICON Far Ultraviolet Instrument (FUV) was conducted (Wautelet et al. 2021). This work already made use of ionosondes and C2 mission as external data, so we focus here on the essentials of each technique. The interested reader will find more details regarding these instruments in the aforementioned reference.

2.1 ICON-EUV

The ICON observatory started main science mode operations on November 16, 2019 and the mission has produced EUV data since then.

EUV is a wide field ($17° \times 12°$) extreme ultraviolet imaging spectrograph designed to provide O^+ density profiles during daytime (Sirk et al. 2017). The spectral range of EUV is 54–88 nm, which includes the OII emission lines at 61.7 nm and 83.4 nm used to infer O^+ density profiles, in addition to the 58.4 nm emission line of HeI. Every 12 s, data product L2.6 provides the daytime O^+ density profile obtained from the inversion of level-1 limb brightness profiles of the 61.7 and 83.4 nm emission lines (Stephan et al. 2017). Each exposure produces a vertical profile of the EUV spectrum and the horizontal information is provided by the motion of the spacecraft. Note that even if the EUV instrument was initially designed to provide level-2 (L2) profiles with a 60 s cadence to fulfill the ICON science requirements, and therefore merging five observation epochs, it has been further decided to perform the inversion on each of the 12 s brightness observations and deliver a L2 profile at that cadence. The forward model that iteratively fits the 61.7 and 86.4 nm emission profiles makes use of the International Reference Ionosphere (IRI) 2007 to provide the range of possible ionospheric profiles (basis set of solutions), in order to retrieve the peak density N_mF_2 and altitude h_mF_2 at convergence. EUV O^+ density profiles also include $[O^+]$ uncertainties for each altitude as well as for h_mF_2 and N_mF_2. The uncertainties in the retrieved parameters originate from the covariance matrix obtained at convergence of the iterative retrieval algorithm. Additionally, L2 data include a quality flag related to the adjustment quality which has to be taken into account when using EUV data. The possible flag values are 0 (no issue reported), 1 (moderate issue) or 2 (severe issue). Several warnings related to a high solar zenith angle, low F10.7 solar flux or low h_mF_2 value at convergence are recorded as flag details in the case of flag=1 or 2. Also available in the L2 data are the adjustment residuals between data and model, measured by the chi-squared (χ^2): depending on internal thresholds, the quality flag can be set to 1 or 2, the latter option meaning that the data should not be used for scientific studies. The geographic location of the EUV profile corresponds to the tangent point location at 300 km altitude, which is approximately the mean value of h_mF_2 for the region covered by ICON. This arbitrary fixed value does not therefore correspond to the actual peak altitude, which induces some inaccuracy on the geolocation of the peak. As a result, coincident measurements may not be exactly "coincident" due to this approximation, although the difference is probably smaller than the window of agreement in location assumed in our methodology (see Sect. 2.5). We use the L2.6 NetCDF files version v03, which is the latest version available at this time.

2.2 Radio-Occultation

The six FORMOSAT-7/COSMIC-2 (further referred to as C2) satellites were launched by the US Air Force Space Test Program into a $24°$ inclination low Earth orbit on June 25, 2019. The primary C2 mission objective is to continuously and uniformly collect atmospheric and ionospheric profiles to improve the quality of weather forecasts, climate studies, and space weather research (Straus et al. 2020). The C2 ionospheric profiles result from the inversion of radio-occultation measurements of GNSS signals observed by a C2 satellite: the primary observable is the Total Electron Content (TEC) profile, *i.e.* a TEC value for each tangent altitude. These quantities are then inverted, assuming a given symmetry in the electron density distribution in the region crossed by the GNSS-C2 lines of sight. Because of the existence of non negligible gradients in N_e, the symmetry is not strictly satisfied and the official inversion technique used for C2 products takes into account the three-dimensional heterogeneity of the electron density plasma (Yue et al. 2011; Chou et al. 2017). This is particularly true in regions where strong gradients occur, like around the equatorial anomaly crests where the fountain effect induce large altitudinal and lat/lon gradients. The Abel inversion method

is therefore "aided" to prevent systematic artifacts due to the application of the classical method to radio-occultation TEC data. This algorithm, which provides the COSMIC-2 electron density profiles used in this study, relies on three-dimensional time-dependent electron density measurements based on the climatological maps constructed from previous observations.

The C2 profiles are therefore the result of the inversion of numerous lines of sight between the C2 spacecraft and the rising or the setting GNSS satellite. As a result, an occultation lasts generally several minutes so that the geographic position of the profile is rough, depending on the occultation geometry. The smear parameter measures the geographic extent related to the different tangent points of a single C2 profile and can range from about 100 km to more than 5000 km. Therefore, C2 profiles do not provide strict N_e altitude profiles as in the case of ionosonde and ISR data.

The quality control of C2 profiles is the same as that implemented in Wautelet et al. (2021) where full details of the methodology can be found. Briefly, each N_e profile is fitted using a 4-parameter Chapman function and is accepted as valid if the observed parameters N_mF_2 and h_mF_2 do not significantly differ from the modeled values:

$$N_e = N_mF_2\, e^{\alpha\left[1 - \frac{(h - h_mF_2)}{H} - e^{-\frac{(h - h_mF_2)}{H}}\right]}$$

with N_e the electron density, N_mF_2 the electron density at the F_2 peak, α the Chapman parameter, h the altitude, h_mF_2 the altitude of the F_2 peak and H the scale height. Note that if observed N_mF_2 and h_mF_2 values are the initial conditions of this iterative process, the final modeled value will always differ from the observed ones.

This modeling ensures that the profiles are reasonably smooth and realistic, and these qualities allow them to be profitably used as a reference in the framework of comparison studies. Note that the threshold "model-observation" values related to the four parameters are defined in Sect. 2.5.

Finally, we note that electron density profiles extracted from the C2 "IonPrf" product are provisional data at the time of writing this study, and that no error bar is available for the density values. To circumvent this difficulty, uncertainty values for N_mF_2 and h_mF_2 will be taken from the literature (see Sect. 4).

2.3 Ionosonde

Vertical incidence soundings performed by ionosondes have been conducted for more than a century, and provide precise and accurate electron density profiles of the bottomside, from the E-region to the F-layer peak. The technique relies on the reflecting properties of an ionized plasma with respect to an incoming electromagnetic wave. For a given altitude, if the wave frequency ω_w is equal to or larger than the plasma frequency ω_p, the wave is reflected back to the ground. Otherwise, the wave keeps on propagating in the medium undergoing refraction, which from magnetoionic propagation theory (e.g., Sen and Wyller 1960) occurs in two principal modes called ordinary and extra-ordinary. During an ionospheric sounding, an emitting antenna sends radio pulses with frequency ranging from 1 MHz up to 15 MHz or greater in the vertical direction while another antenna receives the reflected signals. For the case of vertical soundings, these two antennas are often the same. From this basis, one can compute the travel time of the different pulses, which again through knowledge of magnetoionic propagation allows conversion of delay time into a physical reflecting height with each frequency (with the latter converted into the electron density at that height). Since the

F_2 peak represents the highest electron density in the ionosphere, the highest frequency of reflection provides a direct measure of N_mF_2. These observations are then typically presented using a graphical form called an ionogram, depicting the vertical structure of the ionosphere. The ionograms actually show the travel time of the pulsed signal, translated in distance units, from the transmitter to the receiver and considering a vertical incidence. As this signal always travels more slowly in the ionosphere and back to the receiver than in free space, the observed altitudes, called virtual heights, always exceed the true reflection heights. An inversion algorithm is therefore needed to retrieve the true heights and derive, for instance, that of the peak, *i.e.* h_mF_2. In the frame of this study, we use the SAO-Explorer software developed by Lowell Digisonde International (LDI) which uses the true height inversion algorithm called NHPC (Huang and Reinisch 1996). The manual scaling of an ionogram consists in graphically selecting its important features to allow the inversion algorithm properly retrieving the electron density profile (Piggot and Rawer 1978). More precisely, we actually draw the ionogram trace, associating to each frequency step its virtual height corresponding to the different layers observed on the ionogram. Based on this hand-drawn trace, we then run, in SAO-Explorer, the NHPC algorithm to retrieve the electron density profiles, and hence the peak height and density. The ionosondes constitute therefore a convenient way of measuring F-peak electron density and height over a particular location, with a time resolution that can be as small as 1 or 2 minutes in the case of new-generation facilities. The ionosonde network is made up of several dozens of stations distributed worldwide and whose data can be freely accessed, e.g. via the FTP access provided by the National Oceanic and Atmospheric Administration (NOAA).

In this work, we manually scale raw ionograms to control the quality and the reliability of the data before comparing to EUV measurements. More precisely, for each ionogram of interest, we manually inspect and scale a whole time sequence ranging from 15 minutes before to 15 minutes after the ionogram of interest. This prevents misinterpretation of a particular ionogram, especially if its structure is more complex than the ones before and after, and guarantees the understanding of the underlying physics. It is also a means to reduce the error on N_mF_2 as it follows a natural regular variation with time. Let us also highlight that error bars for electron density values are not available using the scaling software SAO-Explorer. However, as mentioned later in the discussion section, the accurate scaling of the ionograms performed by trained scientists make the uncertainty on f_oF_2 very small, hence on N_mF_2. As for the h_mF_2 uncertainty, it depends on the profile sharpness around the F-peak and has been fixed to the value of 5 km, which is estimated by visual inspection of numerous profiles and their sensitivity to little changes in their ionogram scaling.

We also refer the reader to Wautelet et al. (2021) for more methodological details concerning the ionosonde observations.

2.4 Millstone Hill Incoherent Scatter Radar

Beginning in the late 1950 s to early 1960 s, it became possible to remotely sense altitude dependent profiles of the full ionospheric plasma state from the ground using the technique of collective Thomson scatter, more commonly known as incoherent scatter and pioneered by William Gordon (Gordon 1958). By using a radar technique at VHF frequencies and above which employs a wavelength much less than the plasma's Debye length scale, very weak Bragg backscatter from the random thermal motion of electrons is possible with a megawatt class peak power transmitter and a high gain, large aperture antenna system. The frequency spectrum of the backscattered signal is very rich with information not only on electron density and temperature but also on ion density and temperature, due to electrostatic

effects, and also on bulk plasma velocity (Evans 1969). Furthermore, the very weak nature of the scattered signal means that the Born approximation (Van Hove 1954) is well satisfied, and full altitude profiles can be sensed of the ionospheric plasma state along the radar beam from below the E region to well into the topside ionosphere. However, the size of the radar system and resources required to operate it means that only a currently limited number of stations are available.

Millstone Hill (42.6 N latitude, 288.5 E longitude) has been operated since 1960 as a mid-latitude / subauroral incoherent scatter radar (ISR) at UHF frequencies (far above the HF frequencies used by ionosondes). Supported by the US National Science Foundation as a Geospace Facility, the radar does not operate continuously due to resource limitations but is instead scheduled for a regular series of experiments. Two antennas are employed: a fixed vertical 68 m diameter antenna and a steerable 46 m antenna, which has a field of view encompassing a good portion of the North American longitude sector. This study primarily uses the more sensitive vertically pointing antenna which produces vertical ionospheric profiles, although some off-zenith data is included in the gridded fit producing F_2 height (cf. next paragraph). Such profiles are directly comparable to ICON EUV measurements when orbital geometry dictating the satellite was at its maximum northern location viewing north, and conjunction experiments were selected and executed accordingly.

ISRs use two fundamental resonance modes in the ionospheric plasma, and these are both employed in this F_2 peak region study. The first uses ion-acoustic thermal resonances ("ion line") in the plasma, and provides in particular electron density and other parameters as a function of altitude through a nonlinear fitting process involving a forward model based on first principles plasma theory (Dougherty and Farley 1960). N_mF_2 and h_mF_2 are then calculated as a regularized derived product from the time-dependent F_2 region direct electron density altitude profile. As described e.g. by Zhang et al. (2017), this is accomplished by a least squares fitting procedure performed as part of the standard Millstone Hill Gridded Data product software package (profileFit). The resulting regridded radar data have a standard 15 min cadence and a set of standard altitudes with an altitude-dependent spacing. All local basic-derived parameter data regardless of waveform were processed, including data collected with beams pointed off zenith. Low elevation (<45°) data were excluded. Scalar data including electron density were then fit with a bicubic tensor product spline in time and altitude.

In the experiments reported here, the input altitude resolution across various radar waveforms ranged from approximately 40 km to 72 km and with variable altitude sampling step size ranging from 4.5 km to 36 km. Uncertainties in F_2 peak electron density were then calculated as a byproduct of the spectral and grid fit process. Under the assumptions of the gridded fit mentioned above, uncertainties are estimated statistically at ∼5 percent for N_mF_2 and ∼20 km for h_mF_2. Ion-acoustic resonance measurements of F_2 peak parameters were available at all local times.

The second mode, sampled simultaneously with the "ion line", uses very weak and narrow enhanced Langmuir resonance scatter ("plasma line") whose frequency offset is determined by the altitude dependent ambient plasma frequency in the ionosphere. Normally these lines are extremely weak and undetectable; however, in the presence of fast photoelectrons, their power is increased to the point of detectability (Akbari et al. 2017). The frequency of the Langmuir resonance at the F_2 region density peak is subsequently converted to electron density (with a small correction for nonzero electron temperature, taken from the ion line measurement), and is independent of radar waveform choice since it occurs at an inflection point in the profile. Since the technique measures frequency rather than spectral shape, uncertainty in N_mF_2 is significantly improved over the ion line mode and is

at or better than the 1 percent level at a time cadence of 4 minutes. Due to changes in signal processing techniques during the experiments used here, plasma line derived values of h_mF_2 were not always available and are therefore not used in this study. Note that due to the need for fast photoelectron illumination, this measurement is only available during daylight hours. However, all the experiments in this study met that criterion.

2.5 Comparison Methodology

The aim of this comparison work is the identification of colocated and simultaneous profiles to assess the differences and similarities between ICON-EUV profiles and external datasets. A conjunction, or match, is considered if the geometric distance between two profiles is smaller than 500 km, this maximum distance being computed at a given ionospheric altitude of 300 km. Similarly, both profiles should not differ in time by more than 15 minutes to be considered as synchronized. The choice of these thresholds is a compromise between the sample size (number of matches) and the importance of space and time variability of the ionospheric plasma.

To mitigate the latter effect, we assess for each conjunction the expected variability due to the non-perfect synchronization and co-location using the International Reference Ionosphere (IRI) 2016 model. IRI is evaluated at the location of both EUV and external profiles, and differences between IRI runs allow us to estimate the part due to regular gradients, from a climatological point of view, in the observed differences. These IRI values are then removed from our profile differences, so that the N_mF_2 and h_mF_2 differences analyzed in this paper are considered to be simultaneous and colocated at the IRI level. It is worth noting that these IRI-to-IRI differences most probably underestimate the real difference between the different profile locations and measurement epochs due to the climatological nature of the model, which does not take into account of the daily variability.

The quality control of EUV profiles consists of excluding all profiles for which the internal quality flag is equal to 2. This study includes therefore several cases for which the quality flag is equal to 1, meaning that the interpretation of the results should be careful. To prevent moderate issues in the fitting procedure, we decide to additionally exclude all profiles for which a high χ^2 value triggered a warning message in the flag details, stating that the adjustment quality can be doubtful. This outlier rejection leads to an exclusion of nearly 11% of the total number of matches. Additionally, the profiles with associated warnings reporting low F10.7 or h_mF_2 values have been kept in our analysis because they constitute the bulk of our database, with nearly 99% of the matches. This very large number is explained by the very low solar activity of the analyzed period (December 2019 – March 2021) for which F10.7 index was lower than 80 s.f.u. (Solar flux units) for about 90% of the time. Ongoing analysis has found that the EUV algorithm is properly adjusting for low F10.7 via the two-color fitting scheme, and this warning flag may be removed in future data releases. However, the low h_mF_2 will continue to be flagged due to the separation of the connection between O^+ and electron density, in combination with the reduced radiative transport effects on the 83.4 nm emission that enable the EUV algorithm. These particular conditions have to be taken into account when discussing the limitations of the EUV inversion method.

In addition, we select the C2 profiles that successfully pass our quality control, based on similar filters as previously used in the framework of the FUV comparison (see Wautelet et al. 2021):

- The C2 maximum smear value was fixed to 1500 km, corresponding to the ground trace of EUV tangent points between 150 and 550 km altitude.

Fig. 1 Time coverage available for each external source
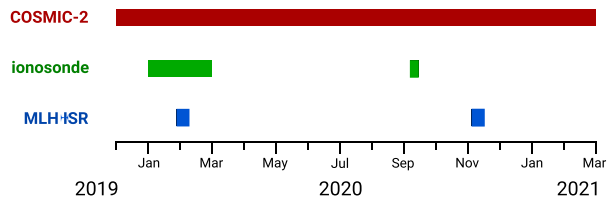
- The threshold values regarding the Chapman-model applied to C2 profiles are the following: $(N_m F_2\, obs. - N_m F_2\, fit) < 5 \times 10^{10}\ e/\text{m}^3$, $(h_m F_2\, obs. - h_m F_2\, fit) < 10$ km, $H \leq 100$ km and $\alpha \leq 2$.

This selection leads to the exclusion of 47% of the total number of EUV-C2 conjunctions.

As described above, Millstone Hill ISR data on F_2 peak parameters are available in both "plasma line" and "ion line" modes for each conjunction since these occurred during daylight hours. Since the first mode is the most precise technique for electron density retrieval but $h_m F_2$ was not always available due to changes in signal processing methods, we therefore compared peak F_2 density values using the "plasma line" measurements while peak F_2 altitudes were obtained from the simultaneous "ion line" dataset.

The time intervals considered in this work differ from one instrument to another. Indeed, if the COSMIC-2 constellation provides several thousands of profiles daily, ionosonde data have to be manually scaled and validated, which requires a lot of work and explains the limited number of comparisons. The ISR data were collected in a campaign mode specifically for ICON EUV comparisons, so that only a limited number of observations are possible. The ionosonde comparisons were performed during the Jan-Feb 2020 period (one day every 3 days) and for 07–11 Sep 2020. The two ISR campaigns used were from Jan, 29 2020 to Feb, 7 2020 and 4–13 Nov 2020 (Fig. 1).

3 F2-Peak Parameters Results

Main comparison results are related to the F_2-peak parameters $N_m F_2$ and $h_m F_2$. Their differences, computed as "EUV minus external data" are detailed in Table 1 that will serve as a basis for a more detailed analysis. EUV-C2 maps of $N_m F_2$ and $h_m F_2$ differences are then presented using magnetic latitude (MLAT) and local time (LT) coordinates.

3.1 Summary Statistics

Table 1 summarizes absolute and relative differences for $N_m F_2$ and absolute difference for $h_m F_2$. One can see that except for the time limited comparison with ionosondes in September 2020, all comparisons show that the EUV $N_m F_2$ value is significantly smaller than that of other data sources. The mean difference with respect to the C2 dataset is about $-3.9E+11$ e/m^3, corresponding to -56%. Turning to the ionosonde comparison, we can see that we get a similar relative result (-52%) but a twice smaller absolute bias of $-1.9E+11$ e/m^3. This absolute difference can be explained by the lower absolute $N_m F_2$ values of the ionosonde dataset due to the ionosonde location, which is mainly mid-latitudes. The two ISR comparisons at Millstone Hill reveal similar relative values (-52% and -68%), despite significantly different absolute bias value of $-1.6E+11$ and $-3.1E+11$ e/m^3. Again, these numbers are explained by a change in the absolute ionization level between both time periods: in November 2020, the solar activity, and so the absolute $N_m F_2$ value, was much larger than during

Table 1 Mean and standard deviation of ionospheric parameter differences between EUV and C2, ionosonde and Millstone Hill ISR radar (MLH)

	N	ΔN_mF_2 [m^{-3}]	ΔN_mF_2 [%]	Δh_mF_2 [km]
EUV - COSMIC-2	38750	-3.9×10^{11}	-56	20
(*Dec 2019 - Mar 2021*)		$+/- 2.6 \times 10^{11}$	$+/- 27$	$+/- 42$
EUV - ionosonde	674	-1.9×10^{11}	-52	15
(*Jan - Feb 2020*)		$+/- 8.4 \times 10^{10}$	$+/- 17$	$+/- 22$
EUV - ionosonde	143	5.1×10^{10}	20	0
(*Sep 2020*)		$+/- 1.4 \times 10^{11}$	$+/- 33$	$+/- 27$
EUV - MLH	120	-1.6×10^{11}	-52	8
(*Jan - Feb 2020*)		$+/- 4.1 \times 10^{10}$	$+/- 11$	$+/- 19$
EUV - MLH	141	-3.1×10^{11}	-68	31
(*Nov 2020*)		$+/- 1 \times 10^{11}$	$+/- 15$	$+/- 62$

the early months of the same year (see Fig. 4c and e). In conclusion, if the absolute value of the difference changes according to the background value, the relative N_mF_2 differences with respect to multiple external data sources seem to converge to a mostly constant value of -55% on the average.

We note that the standard deviation of the absolute differences in N_mF_2 appearing in Table 1 are smaller for specific limited comparisons performed using ionosondes and MLH radar: their magnitude is around 1E+11 e/m^3 when the standard deviation related to the C2 dataset is about twice larger. The ionosonde and ISR comparisons, though limited in time, provide more precise comparisons than the C2 dataset for which the standard deviation value reflects the whole observation period. As being significantly different from other comparison datasets, the case of the September 2020 ionosonde comparison suggests however that N_mF_2 differences can vary with time. This possibility will be investigated in the discussion section, where the stability of the daily differences is discussed.

Additionally, h_mF_2 differences are all positive, ranging from 0 to 31 km on average, meaning that EUV retrievals produced higher peak altitudes than the other data sources. The lowest discrepancies are found for ionosonde comparisons when the largest ones have been observed in November 2020 for MLH radar comparisons, with a mean peak height difference of 31 km and an associated standard deviation of 62 km. In contrast to density values which are proportional to the background value, it is more difficult to explain the difference in peak height at the same location (Millstone Hill facility) between different epochs of the year. Day-to-day variability of peak density and height should therefore be investigated to understand such observations (see the discussion section).

Given the consideration for long-term systematic changes in sensor and algorithm performance, the Jan-Feb 2020 comparison in Table 1 represents a sufficient sampling of data covering more than one full orbit precession cycle, sampling all locations and local times, to evaluate the performance of the EUV compared to mission requirements for precision in h_mF_2 and N_mF_2. These are represented as such in Table 1 by the 1σ range in spread of the distributions. Additionally, the EUV-ionosonde comparison from Jan-Feb 2020 provides the largest number of samples to best evaluate this statistical distribution. For this span, our comparison shows a spread of 17% in N_mF_2 which meets the ICON requirement of 20%, and 22 km in h_mF_2 which is larger than the ICON requirement of 20 km but in line with the requirement when the uncertainties in the ionosonde measurements are properly included in
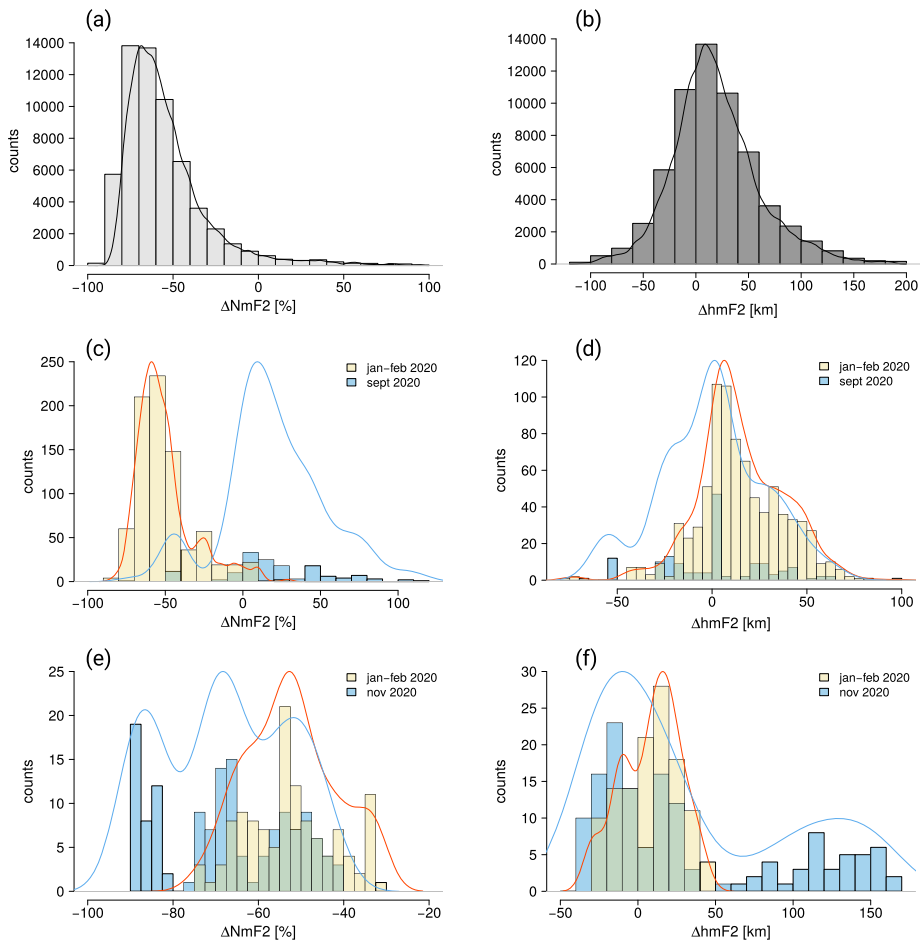
Fig. 2 Histograms and their related kernel density estimation (KDE) of $\Delta N_m F_2$ and $\Delta h_m F_2$ between EUV and C2 (**a** and **b**), between EUV and ionosondes (**c** and **d**), and between EUV and Millstone Hill incoherent scatter radar (**e** and **f**). Sub-figures (**c**) to (**f**) contain two histograms and KDEs which are related to the different time periods analyzed for ionosonde and ISR datasets (see Table 1)

the comparison. These are also considered upper-thresholds of the algorithm performance because this analysis has not filtered any data based on the reported uncertainties in the EUV products. As presented in more detail by Stephan et al. (2022), lower $h_m F_2$ ionospheres that often occur at earlier local times and higher magnetic latitudes will generally yield larger uncertainties in product values because the method becomes increasingly insensitive to ionospheric effects, and thus are likely to contribute more significantly to an overall lower precision of the entire data set. These factors are not considered in this evaluation.

Figure 2 depicts histograms of the relative differences for $N_m F_2$ (left column) and absolute difference for $h_m F_2$ (right column) for C2 (top row), ionosondes (middle row) and MLH radar (bottom row). For mostly all datasets, histograms show a non-Gaussian distribution for relative density values with a linear behavior on the left side of the peak, while $\Delta h_m F_2$ are normally distributed around their mean value. The normal distribution gives confidence to standard deviation values reported in Table 1 which accurately represent, together

with the mean value, the statistical distribution of the variable of interest. The bell shape is more obvious for a large dataset such as the C2 one than for a couple of comparison profiles as for ISR comparisons, where several peaks in $\Delta N_m F_2$ can be observed, especially for the case of November 2020 comparison. In the latter case, the conjunctions have been computed during several consecutive days, with varying local time due to the ICON orbit precession. For a fixed geographic station, the presence of multiple peaks would be explained by a local time dependence but also probably by the rapid though moderate increase of the ionospheric background value due to the F10.7 index growing from 86 to about 92 s.f.u. within three days (4–6 Nov). We also highlight the secondary peak around 125 km for $\Delta h_m F_2$ appearing in the ISR comparison in November 2020 (Fig. 2f), which represents very large discrepancies that need to be further investigated.

3.2 COSMIC-2 Difference Maps

Since local time would probably impact the magnitude of F-peak parameters differences, we investigate its influence, together with that of magnetic latitude using MLAT/LT maps (Fig. 3). All observations within each bin are averaged, with a 30 min resolution for local time and 5° in MLAT. This study is only possible with the C2 dataset as the thousands of conjunctions are regularly distributed in MLAT and LT, unlike fixed ground-stations for which the information is too sparse to create similar maps. For peak density (top plot), we can observe a mostly constant bias of -50 to -60%, except from 16:00 LT between 20° and 40° MLAT, *i.e.* above the northern crest of the equatorial anomaly, where slightly reduced relative values around -25% clearly appear. We can also distinguish slightly lower values above 20° MLAT, generally during daytime starting from 10:00 LT. Similar observations cannot be performed in the southern hemisphere owing not only to the inclination
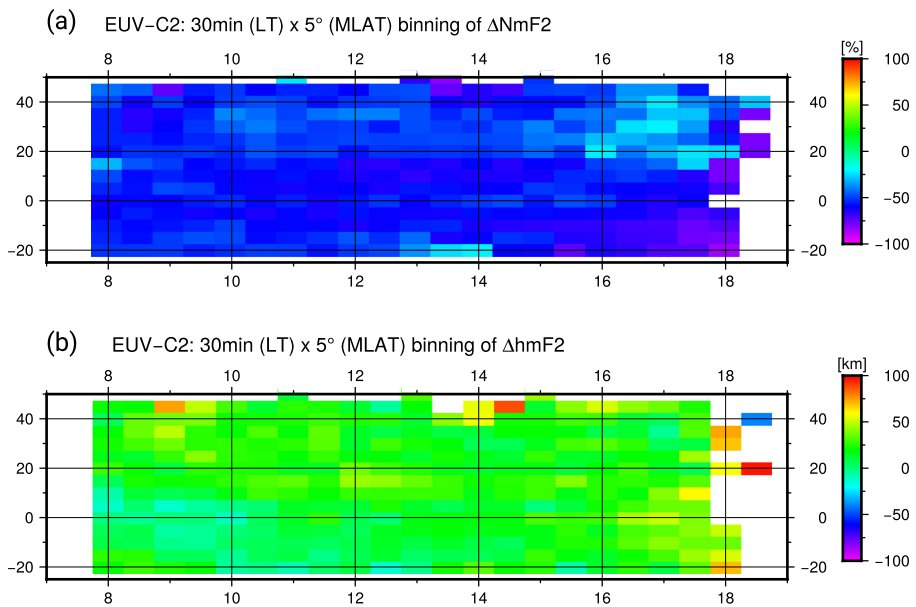

Fig. 3   30 min (LT) × 5° bins (MLAT) of averaged $\Delta N_m F_2$ (**a**) and $\Delta h_m F_2$ (**b**) for EUV - C2 comparison. The map is expressed in local time (LT) and magnetic latitude (MLAT) of the retrieval at 300 km altitude

of the geomagnetic equator with respect to the geographic one but also to the orientation of the EUV to view that is normally toward the north with respect to the ICON orbit, viewing to the south during special mission operations to observe the magnetic conjugate regions. Additionally, we note the very strong negative values at all MLAT bins around the evening terminator (18:00 LT), a condition that may be influenced by the high solar zenith angles, although it may also be that some part of the large EUV field of view intersected the terminator in the darkness, either of which can cause complications with fitting during the inversion procedure. In addition, the pre-reversal enhancement in the electric field could play a role in producing larger differences between the two techniques. More careful investigations based on specific cases should be undertaken to explain these large differences.

$\Delta h_m F_2$ seem to be randomly distributed over the map, with slightly positive values reflecting the mean value of 20 km (Table 1). Few magnetic or local time dependence can be identified here based on Fig. 3b, except the slight negative values describing a line starting from (08:00 LT;10° MLAT) and ending around (12:00 LT;-20° MLAT). This linear pattern can also be seen in the $\Delta N_m F_2$ map, where similar small enhancements (light blue) with respect to the −56% average can be observed.

4 Discussion

Non-zero differences in $N_m F_2$ and $h_m F_2$ have been reported in the previous sections for nearly all dataset comparisons. As each measurement is affected by noise and instrumental errors, it is worth investigating whether these differences are significant from a statistical point of view. Indeed, even in the framework of perfect profile colocation, combining results originating from several instruments having their own precision and accuracy is always challenging. Uncertainties are provided with EUV and MLH $N_m F_2$ and $h_m F_2$ measurements while they are not available for C2 and ionosonde measurements (see Sect. 2). For the latter datasets, we therefore use the values cited in the literature to compute confidence intervals around the peak parameters. Conducting a comparison between C2 and ionosondes, Cherniak et al. (2021) found RMS $f_o F_2$ differences of 0.5 MHz and 2 km (mid-latitudes) to 5 km (low latitudes) mean differences for $h_m F_2$. In the present study, we therefore consider the C2 $N_m F_2$ standard deviation being equal to 0.5 MHz, further translated in electron number density, and that of $h_m F_2$ to 5 km. For ionosonde measurements, we consider that the $f_o F_2$ value is accurate to 0.1 MHz, as being the result of the manual inspection performed by a trained specialist. Standard deviation of ionosonde-derived $h_m F_2$ has also been determined to be 5 km, which is larger than the actual altitude resolution provided by the modern facilities. To investigate whether two peak values significantly differ from each other, we are testing if their own confidence intervals, computed at 95% confidence level, are overlapping. If not, the peak values are considered to be statistically different from each other under a 95% confidence level. In the case of the EUV-C2 comparison, the percentage of non-significant $N_m F_2$ differences is merely 2%, meaning that the average relative difference of −56% is statistically significant for the vast majority of the conjunctions. For $h_m F_2$, an overlap is observed for 32% of the conjunctions, meaning that about two thirds of the observed differences (20 km on average) are significant at 95% confidence level. Applying the same methodology to the ionosonde comparison dataset leads to similar conclusions for the Jan-Feb 2020 period, with a bit less than 2% of the $N_m F_2$ differences and 56% of $h_m F_2$ differences which are not significant. These results confirm the conclusions drawn for the EUV-C2 comparison, being that a significant bias of about −55% is observed for $N_m F_2$

while the situation for h_mF_2 differences is not as straightforward. Additionally, ISR comparisons reveal that 100% of the N_mF_2 differences are statistically significant, considering the quantitative error bounds on both variables. Since in particular the "plasma line" derivation of N_mF_2 is based on a frequency measurement and the value of physical constants within the warm plasma frequency formula, ISR data provide a particularly robust and quantitatively accurate uncertainty in the context of these comparisons. The significance level of h_mF_2 EUV-ISR differences is found to be observed for about 32% of cases in Jan-Feb 2020 and 72% for Nov 2020 period, given the 1-sigma h_mF_2 uncertainty of 20 km for the MLH ion line measurement. This is sufficient for accurate comparison, and due to the weak nature of incoherent scatter mentioned earlier the results have information from full altitude profiles beyond the F_2 peak. This means it provides F_2 peak height determinations that are based on directly observed profile shape above and below the peak, unlike ionosonde measurements which can only sense the bottomside from the ground and which rely on further analysis to translate virtual height into actual height. To summarize, given a confidence interval of 95%, the bulk of comparisons show a significant difference between -50% and -60% in the EUV N_mF_2 values while a small positive offset in the EUV peak altitude of 10-20 km is probable. We note as well that two datasets do not lead to similar conclusions: the September 2020 ionosonde dataset and November 2020 Millstone Hill ISR dataset. Both cases will be investigated in more detail in the next paragraphs.

As already mentioned in Sect. 2.5, numerous EUV profiles with a quality flag equal to 1 are part of our comparison database. Indeed, for a very large proportion of them, a very low solar flux is pointed out as a warning that a corresponding systematic error may exist in the data products for the reasons already mentioned. It is therefore worth investigating whether the F10.7 value impacts the comparisons with respect to the accuracy of the results. Because it is available for the whole comparison time period, we consider the C2 dataset only, from which we extract and analyze a subset with F10.7 larger than 80 s.f.u. We compute statistics similar to those shown in Table 1 on this reduced dataset counting 45 days only, instead of 489 previously. The mean N_mF_2 absolute difference is larger than for the whole dataset, with $-5.3E+11$ $(+/- 2.4E+11)$ e/m^3, and the relative difference is found to be -62% $(+/- 18\%)$. With respect to the whole dataset, a larger absolute value was expected as increased F10.7 values induce larger absolute N_mF_2 values. However, we point out that the relative difference is still slightly larger than for the whole dataset, with -62% instead of -56%, with a smaller standard deviation value reflecting more reliable statistics. However, note that the EUV inversion algorithm outputs a bias term whose aim is to compensate for a biased atmospheric scaling (Stephan et al. 2017). Ongoing analysis has examined this concern and found that the retrieval method does appear to be properly compensating for this factor and it is expected future releases of the data will remove this warning flag (Stephan et al. 2022).

In the previous paragraphs, it has been suggested that ΔN_mF_2 and Δh_mF_2 would depend on background conditions, *i.e.* absolute N_mF_2, but also probably on other hidden variables. Indeed, N_mF_2 simultaneously depends not only on the magnetic region (electron density peak values strongly depend on MLAT) but also on solar activity. Figure 4 shows the times series of the daily values of ΔN_mF_2 and Δh_mF_2, together with MLAT, the absolute N_mF_2, the F10.7 index and the Disturbed Storm Time (DST) index for the EUV-C2 dataset. The time series of ΔN_mF_2 shows a complex behavior, including wave-like oscillations like for the January-February 2020 period, in addition to a long-term non-linear trend. For Δh_mF_2, we observe similar oscillations but no net trend is visible on the figure. Let us however point out that within one month in August 2020, the EUV-C2 Δh_mF_2 daily difference drops from about 100 km to 0 km. Although this pattern is in phase with the mean MLAT drop during this month, due to the combination of ICON and C2 orbit precession, we previously

demonstrated that MLAT is not a major factor explaining $\Delta h_m F_2$ and $\Delta N_m F_2$ differences (see Fig. 3). This example of August 2020 is reproduced with a smaller amplitude at several occasions in the time series, when rapid changes of the EUV-C2 differences are recorded. The fact that daily differences can strongly vary from one epoch to another may explain why the September 2020 ionosonde dataset showed results different from other datasets, without however providing any explanation for that result. The impact of geomagnetic activity at equatorial latitudes, monitored by the DST index (Fig. 4f), does present several time fluctuations, especially during Fall 2020: three moderate drops are clearly identified around September, October and November. Let us however note that a DST decrease of about -50 nT generally translates moderate geomagnetic disturbances, such as those due to recurrent coronal holes or induced by minor flares facing Earth. Although the multiple DST drops in Aug.-Sep. are of moderate still significant intensity, it seems that they do not produce any direct effect on F-peak parameter differences. Substantial changes in $\Delta h_m F_2$ and $\Delta N_m F_2$ differences are indeed observed during very quiet periods of geomagnetic conditions while disturbed ones do not imply an increased level of disagreement between EUV and C2. Even if a more detailed correlation analysis using time lag would be appropriate to completely exclude the geomagnetic activity from the explaining variable list, it is clear from Fig. 4 that it does not constitute the main driver of the observed variability. Therefore, neither the $N_m F_2$ background, related to F10.7 index, nor the MLAT, nor the geomagnetic activity was successful in explaining the $\Delta h_m F_2$ and $\Delta N_m F_2$ differences that could arise from transient contamination of the data, or with actual detector conditions that significantly differ from the calibrated values. For EUV, the calibration relies on two independent steps: the flat fielding and the absolute lunar calibration (see dedicated paragraph below). While the first one aims at correcting for inhomogeneous sensitivity and optical properties over the detector plane, the second one monitors the absolute photometry needed to accurately retrieve the O^+ density value. Most simply, $h_m F_2$ is driven by the shape of the altitude profile and so is affected more by the flat-field, while $N_m F_2$ is driven more by the absolute intensity and so is affected most by the radiometric calibration.

In addition to peak parameters comparison, we also compare the topside density values obtained from EUV and C2. Note that this analysis is not possible for ionosondes, as they do not provide actual profiles above the density peak. Such an analysis is possible for MLH ISR data as that directly observes the topside, but such comparisons are beyond the scope of this study. For each altitude ranging from 450 to 600 km altitude, we compute the EUV-C2 $[O^+]$ difference at each 5 km altitude step. We then compute the mean and the standard deviation of these differences for each conjunction in order to investigate any bias and variability in $[O^+]$ at these altitudes. Similarly to peak parameter analysis, the mean value translates the presence of a systematic difference between the profiles, *i.e.* a bias, while the standard deviation assesses the standard agreement of each profile to the mean. Although, if O^+ remains the major ion at these altitudes, the contribution of H^+ and He^+ becomes significant so that we need to subtract them to compare C2 profiles, which represent N_e, with EUV profiles monitoring O^+ density. To that purpose, we use the IRI model to compute, for each altitude step, the abundance ratio, *i.e.* the fraction of the different ions to their total amount, which is equal to N_e due to plasma electro-neutrality. Over the whole C2 dataset, the mean absolute difference is equal to $-5.927\text{E}+10$ e/m^3 while the corresponding relative value is -27%. The mean standard deviation over the whole time interval is $1.7\text{E}+10$ e/m^3. However, these values significantly evolve with time, as shown in the time series of Fig. 5. We can observe similarities with Fig. 4a, for instance cycles and long-term trend in the mean value (Fig. 5a). It is interesting to note that standard deviation time series shows cycles that have approximately the same period as the orbital cycles observed in the MLAT time
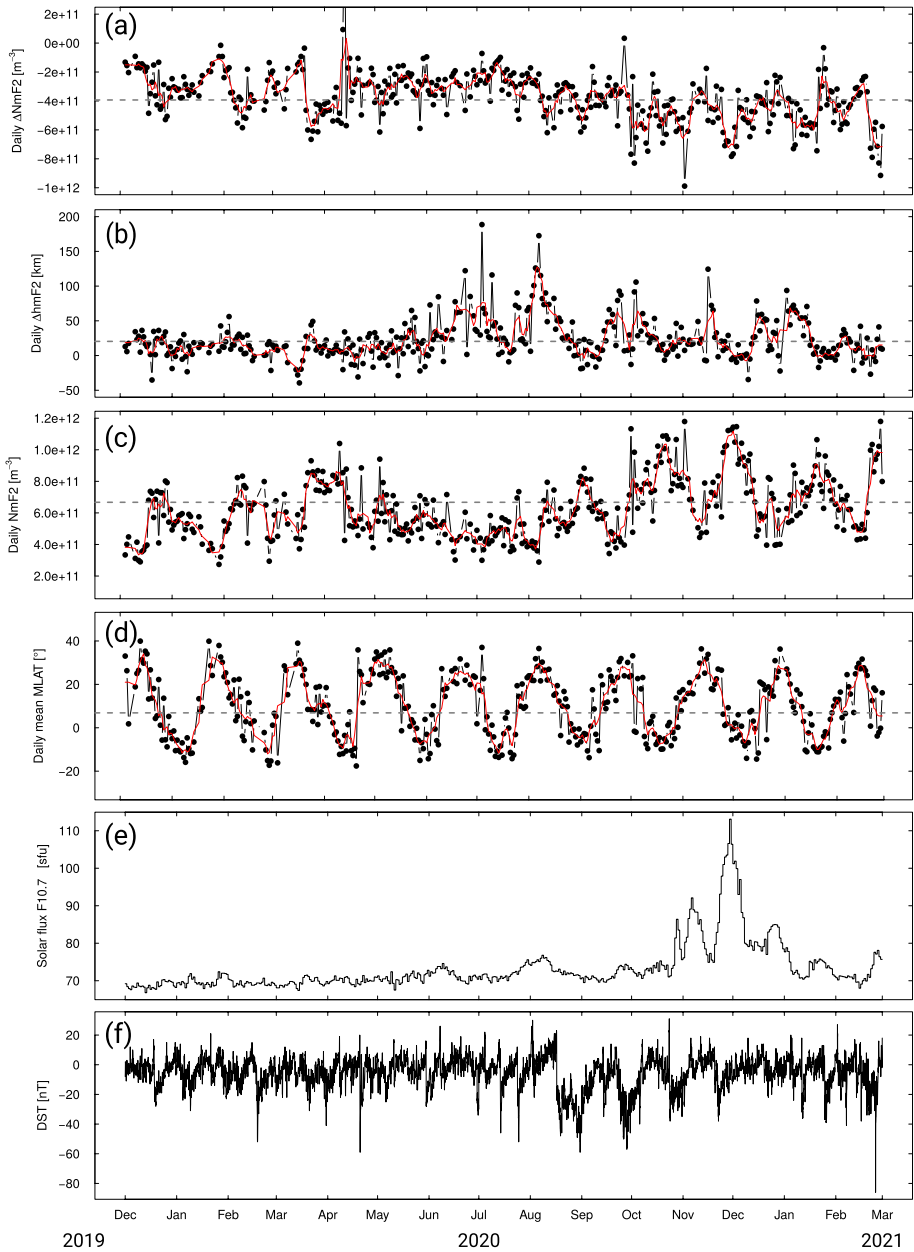
Fig. 4 EUV - C2 comparison: (**a**) time series of daily $\Delta N_m F_2$ values, (**b**) $\Delta h_m F_2$, (**c**) $N_m F_2$, (**d**) MLAT, (**e**) Solar flux F10.7 and (**f**) DST index from December 2019 to March 2021. Red lines are smoothed values computed on five-days running averages. Dashed lines are the average values computed over the whole times series

series (Fig. 4d): larger variability is observed for low-latitude matches, for instance at the beginning of January 2020, mid-Feb 2020 and beginning of April 2020. This indicates that
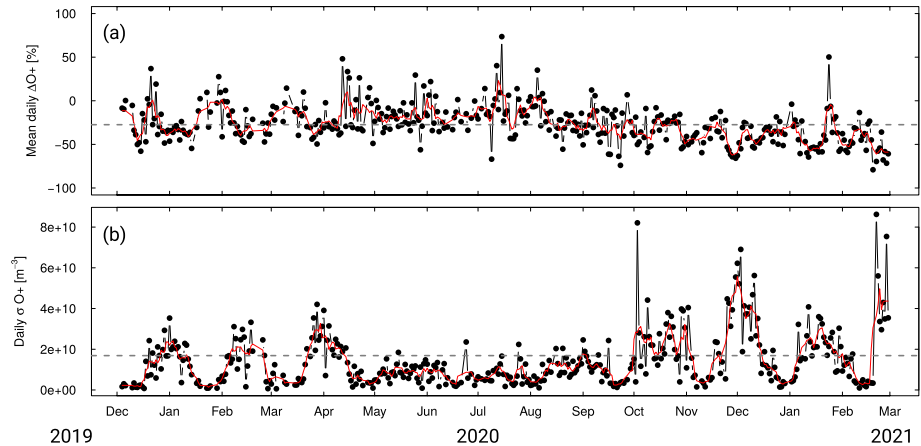
Fig. 5 EUV - C2 comparison between 450 and 600 km altitude (topside): time series of the daily mean difference (**a**) and of the standard deviation (**b**) of the O$^+$ density profile differences from December 2019 to March 2021

the disagreement level between topsides is larger above the equatorial crests than in the mid-latitude regions. At last, the mean relative bias between topsides is much smaller than for N_mF_2: we find a -27% difference at high altitudes, whereas -56% was found for the peak. This may be due to the fact that most of peak comparisons are related to very low h_mF_2 values. In such a case, the 83.4 nm photon source is close to the region where it is later resonantly scattered (in the F-peak), which may result in ambiguities which are more complicated to untangle by the inversion. In the topside, the source and scattering regions are more clearly separated, which could result in reducing the differences between EUV and C2 profiles. Also, reduced differences in the topside region with respect to peak values could be associated with relative sensitivity of low and high altitude pixels in the detector, which is related to the flat fielding procedure discussed in the next paragraph.

To determine accurate density profiles from the EUV emission lines requires that there are no systematic errors in the relative detector sensitivity along the tangent altitude profiles, and that the look direction of the spectrograph is known to within 0.1 degree. Knowledge of the absolute photometric throughput is also important although not as critical as the relative line shapes. To ensure correct calibration the EUV instrument is pointed monthly at the nadir with the solar zenith angle close to zero. These data are used to create time-dependent flat-field images for each emission feature. In Fig. 6 we present raw (black) and flat-field corrected (red) profiles for O–83.4 nm and O–61.7 nm obtained at the beginning of the mission, and 54 weeks later. After applying the flat-field, the line shapes are restored to their beginning-of-mission state. To verify absolute throughput the EUV spectrograph is regularly pointed at the Moon when the phase is within one day of full. Absolute throughput at the 83.4 and 61.7 nm features as determined from Lunar pointings shows scatter of 5 and 10%, respectively. The 61.7 nm feature has shown no loss in throughput whereas the 83.4 nm line has dropped to 0.2 of its original value over 600 days. We fit this gain loss as a function of time with a second order polynomial and adjust the O 83.4 nm accordingly. Thus the scatter observed in throughput obtained from the individual Lunar observations is not imparted on the Level 1 fluxes. These pointings are compared directly to near-contemporaneous Solar Dynamics Observatory Extreme Ultraviolet Experiment spectra V6 (Woods et al. 2012). Analysis of these data (Sirk et al. in prep.; Korpela et al. in prep.), and the solar models
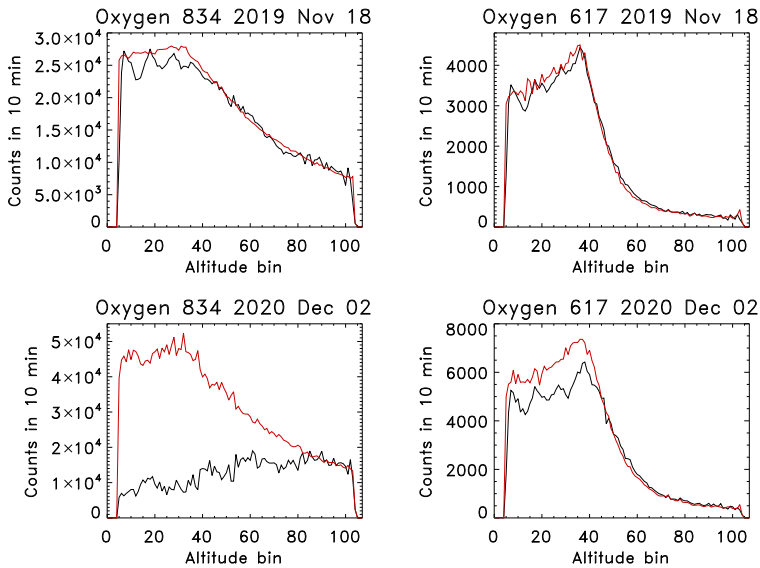
Fig. 6 Raw detector O–83.4 and 61.7 nm line profiles in units of counts obtained over 10 minutes near local solar noon (black) for the beginning-of-mission (top panels) and 54 weeks later (bottom panels). Overplotted (in red) are the same data after application of the appropriate flat-field. In spite of a loss in detector gain of ∼60% in the O–83.4 nm line the corrected 2020 profiles have the same shape as they did at the start of the mission

NRLSSI-2 (Lean et al. 2011) and FIMS2 (P. Chamberlin, 2020, private communication) show that the uncertainty in ICON EUV throughput is about 25%. Additionally, the Lunar observations show 0.07 degree RMS uncertainty in pointing knowledge which, when combined with a known pointing offset, corresponds to a ∼6 km error at 200 km tangent altitude.

Extensive simulations have been conducted prior to and during the early phases of the ICON mission to evaluate the potential impact of systematic errors, either in the measured data via calibration uncertainties, or in the model from such sources as in errors in fundamental photoionization and absorption cross sections. The results of these simulations showed consistency with the results that are presented here. These simulations found that the algorithm is particularly sensitive in N_mF_2 to such systematic errors. Errors in h_mF_2 were less significant, as this is more significantly driven by the shape of the measured profile that would not be impacted as severely by such systematic errors. However, it is noteworthy that these simulations found agreement with the results presented here, in that the offsets in these parameters were anticorrelated. These results were also consistent with the order of magnitude differences found in this study. As such, a systematic error on the order of 10% can result in offsets in N_mF_2 on the order of 50%, and in h_mF_2 in the exact range of 10-30 km found in this examination of the EUV products. If derived entirely from the calibration uncertainty, these results suggest the sensitivity is underestimated, which returns a correspondingly brighter absolute intensity that is interpreted as a lower ionospheric O^+ density. The complexity of factors in the forward model make these less straightforward to assess.

5 Conclusion

We present the first comparison of daytime O^+ density profiles provided by the ICON-EUV instrument with external dataset including the radio-occultation mission COSMIC-2, ground-based ionosondes and incoherent scatter radar (ISR). The time interval covered by the COSMIC-2 dataset spans from mid-November 2019 to March 2021, while two conjunction campaigns have been considered for each of the ionosonde and ISR dataset, in 2020 and 2021. EUV profiles as well as external data are rigorously selected during the quality control step, preventing results from being contaminated by outliers and spurious data. The EUV peak density N_mF_2 is significantly smaller by about 50% to 60% on average with respect to other datasets, except for some punctual comparisons with ionosondes and ISR. The EUV peak height h_mF_2 is slightly larger by 10 to 20 km with respect to other instruments, which is the same order of magnitude than the uncertainty of the parameter measurement by the other techniques. These results are consistent with a 10% systematic error in either the data or the model, or a combination of both, well within the expected confidence levels of either of these factors in the determination of the accuracy of the EUV products. These differences do not significantly depend on magnetic latitude nor on local time, except that late afternoon N_mF_2 values at mid-latitudes seem less biased than elsewhere during daytime. This could be explained by a favorable line of sight geometry which does not cross the equatorial crests, allowing the spherical symmetry hypothesis to be particularly valid for the Abel inversion. Daily differences of peak density and height are however quite variable with time, suggesting effects due to the ICON orbit precession, precision of the calibrations or technical limitations of the inversion due to sustainably exceptionally low solar activity conditions encountered during the ICON mission. Indeed, the time period covered by this study corresponds to the very deep solar minimum of 2019–2020 which induced F10.7 and h_mF_2 values lower than expected, which pushed the inversion software to its limits, and thus degrades the precision of the retrievals. Better comparison results are expected as soon as higher solar activity periods, e.g. Spring 2022, would be encountered. Despite the challenging physical conditions under which the ICON EUV has completed these remote sensing measurements, we have found that the ICON EUV is still obtaining daytime ionospheric characteristics that meet the mission requirements for precision in N_mF_2 of 20% and in h_mF_2 of 20 km. Future investigations should address the understanding of the causes of the variability observed for N_mF_2 and h_mF_2 differences, for instance with the help of a principal component analysis applied to the numerous factors that can potentially influence the retrieval accuracy. Also, to prevent any drift in O^+ density values with time, it is important to regularly monitor the flat fielding and photometric calibration to counter the effect of instrument ageing. This will ensure the EUV compatibility with external dataset, in order to assimilate ICON-EUV O^+ profiles in physical models. At last, let us highlight that EUV provides, from a single autonomous platform in space, ionospheric peak heights with an accuracy level compatible with that of existing radio-based data, such as ionosondes, ISR and GNSS radio-occultation observations. From this standpoint, the airglow remote sensing method used by EUV represents a major asset, in comparison to GNSS radio-occultation data, for instance, which needs much more infrastructure in space (GNSS and LEO satellites) and at the ground-level, consisting in several multiple stations controlling the space segment. This standalone nature makes easier the transposition of the EUV technology to the future study of other planets ionosphere, like Mars or Venus.

Declarations

Competing Interests The authors declare no competing interests.

References

Akbari, H, Bhatt, A, La Hoz, C, Semeter, JL (2017) Incoherent scatter plasma lines: observations and applications. Space Sci Rev 212(1):249–294. https://doi.org/10.1007/s11214-017-0355-7

Cherniak, I, Zakharenkova, I, Braun, J, Wu, Q, Pedatella, N, Schreiner, W, Weiss, J-P, Hunt, D (2021) Accuracy assessment of the quiet-time ionospheric F2 peak parameters as derived from COSMIC-2 multi-GNSS radio occultation measurements. J Space Weather Space Clim 11:18. https://doi.org/10.1051/swsc/2020080

Chou, MY, Lin, CCH, Tsai, HF, Lin, CY (2017) Ionospheric electron density inversion for Global Navigation Satellite Systems radio occultation using aided Abel inversions. J Geophys Res Space Phys 122(1):1386–1399. https://doi.org/10.1002/2016JA023027

Dougherty, J, Farley, D (1960) A theory of incoherent scattering of radio waves by a plasma. Proc R Soc Lond Ser A, Math Phys Sci 259(1296):79–99

Evans, J (1969) Theory and practice of ionosphere study by Thomson scatter radar. Proc IEEE 57(4):496–530

Gordon, WE (1958) Incoherent scattering of radio waves by free electrons with applications to space exploration by radar. Proc IRE 46(11):1824–1829

Huang, X, Reinisch, BW (1996) Vertical electron density profiles from the digisonde network. Adv Space Res 18(6):121–129. https://doi.org/10.1016/0273-1177(95)00912-4

Kamalabadi, F, Qin, J, Harding, BJ, Iliou, D, Makela, JJ, Meier, RR, England, SL, Frey, HU, Mende, SB, Immel, TJ (2018) Inferring nighttime ionospheric parameters with the far ultraviolet imager onboard the ionospheric connection explorer. Space Sci Rev 214(4):70. https://doi.org/10.1007/s11214-018-0502-9

Korpela, EJ, Sirk, MM, Edelstein, J, McPhate, JB, Tuminello, RM, Stephan, AW, England, SL, Immel, TJ (in preparation) In-flight performance of the ICON EUV spectrograph. Space Sci Rev

Lean, JL, Woods, TN, Eparvier, FG, Meier, RR, Strickland, DJ, Correira, JT, Evans, JS (2011) Solar extreme ultraviolet irradiance: present, past, and future. J Geophys Res 116:A01102. https://doi.org/10.1029/2010JA015901

Mende, SB, Frey, HU, Rider, K, Chou, C, Harris, SE, Siegmund, OHW, England, SL, Wilkins, C, Craig, W, Immel, TJ, Turin, P, Darling, N, Loicq, J, Blain, P, Syrstad, E, Thompson, B, Burt, R, Champagne, J, Sevilla, P, Ellis, S (2017) The Far Ultra-Violet imager on the ICON mission. Space Sci Rev 212(1):655–696. https://doi.org/10.1007/s11214-017-0386-0

Piggot, WR, Rawer, K (July 1978) U.R.S.I. handbook of ionogram interpretation and reduction. Revision of Chaps. 1-4. Technical Report UAG-23A, World Data Center A for Solar-Terrestrial Physics, Warsaw, Poland. Revison adopted by U.R.S.I. Commission III

Sen, HK, Wyller, AA (1960) On the generalization of the Appleton-Hartree magnetoionic formulas. J Geophys Res 65(12):3931–3950. https://doi.org/10.1029/JZ065i012p03931

Sirk, MM, Korpela, EJ, Ishikawa, Y, Edelstein, J, Wishnow, EH, Smith, C, McCauley, J, McPhate, JB, Curtis, J, Curtis, T, Gibson, SR, Jelinsky, S, Lynn, JA, Marckwordt, M, Miller, N, Raffanti, M, Van Shourt, W, Stephan, AW, Immel, TJ (2017) Design and performance of the ICON EUV spectrograph. Space Sci Rev 212(1):631–643. https://doi.org/10.1007/s11214-017-0384-2

Sirk, MM, Korpela, EJ, Stephan, AW (in preparation) The lunar albedo and phase function in the EUV. Space Sci Rev

Stephan, AW, Korpela, EJ, Sirk, MM, England, SL, Immel, TJ (2017) Daytime ionosphere retrieval algorithm for the Ionospheric Connection Explorer (ICON). Space Sci Rev 212(1):645–654. https://doi.org/10.1007/s11214-017-0385-1

Stephan, AW, Meier, RR, England, SL, Mende, SB, Frey, HU, Immel, TJ (2018) Daytime O/N2 retrieval algorithm for the ionospheric connection explorer (ICON). Space Sci Rev 214(1):42. https://doi.org/10.1007/s11214-018-0477-6

Stephan, AW, Sirk, MM, Korpela, EJ, England, SL, Immel, TJ (2022) Characterization of the daytime ionosphere with ICON EUV airglow limb profiles. Space Sci Rev

Straus, P, Schreiner, W, Santiago, J, Talaat, E, Lin, C-L (March 2020) FORMOSAT-7/COSMIC-2 TGRS space weather provisional data release 1. Technical report, NOAA, USAF and NSPO

Van Hove, L (1954) Correlations in space and time and Born approximation scattering in systems of interacting particles. Phys Rev 95(1):249

Wautelet, G, Hubert, B, Gérard, J-C, Immel, TJ, Frey, HU, Mende, SB, Kamalabadi, F, Kamaci, U, England, SL (2021) First ICON-FUV nighttime NmF2 and hmF2 comparison to ground and space-based measurements. J Geophys Res Space Phys 126(11):e2021JA029360. https://doi.org/10.1029/2021JA029360

Woods, TN, Eparvier, FG, Hock, R, Jones, AR, Woodraska, D, Judge, D, Didkovsky, L, Lean, J, Mariska, J, Warren, H, McMullin, D, Chamberlin, P, Berthiaume, G, Bailey, S, Fuller-Rowell, T, Sojka, J, Tobiska, WK, Viereck, R (2012) Extreme ultraviolet Variability Experiment (EVE) on the Solar Dynamics Observatory (SDO): overview of science objectives, instrument design, data products, and model developments. Sol Phys 275:115–143. https://doi.org/10.1007/s11207-009-9487-6

Yue, X, Schreiner, WS, Lin, Y-C, Rocken, C, Kuo, Y-H, Zhao, B (2011) Data assimilation retrieval of electron density profiles from radio occultation measurements. J Geophys Res Space Phys 116(A3). https://doi.org/10.1029/2010JA015980

Zhang, S-R, Erickson, PJ, Zhang, Y, Wang, W, Huang, C, Coster, AJ, Holt, JM, Foster, JF, Sulzer, M, Kerr, R (2017) Observations of ion-neutral coupling associated with strong electrodynamic disturbances during the 2015 st. Patrick's day storm. J Geophys Res Space Phys 122(1):1314–1337